Molecular Cancer Therapeutics

Time-Course Imaging of Therapeutic Functional Tumor Vascular Normalization by Antiangiogenic Agents

Qingbei Zhang, Vytas Bindokas, Jikun Shen, et al.

Updated Version	Access the most recent version of this article at: doi:10.1158/1535-7163.MCT-11-0008
Supplementary Material	Access the most recent supplemental material at: http://mct.aacrjournals.org/content/suppl/2011/05/17/1535-7163.MCT-11-0008.DC1.html

Cited Articles	This article cites 35 articles, 17 of which you can access for free at: http://mct.aacrjournals.org/content/10/7/1173.full.html#ref-list-1

E-mail alerts	Sign up to receive free email-alerts related to this article or journal.
Reprints and Subscriptions	To order reprints of this article or to subscribe to the journal, contact the AACR Publications Department at pubs@aacr.org.
Permissions	To request permission to re-use all or part of this article, contact the AACR Publications Department at permissions@aacr.org.

Time-Course Imaging of Therapeutic Functional Tumor Vascular Normalization by Antiangiogenic Agents

Qingbei Zhang[1], Vytas Bindokas[5], Jikun Shen[2], Hanli Fan[1],
Robert M. Hoffman[6,7], and H. Rosie Xing[1,3,4]

Abstract

We describe here new technology that enables noninvasive imaging of therapeutic functional normalization of tumor blood vessels by antiangiogenic agents. Noninvasive variable-magnification *in vivo*-fluorescence imaging as well as fluorescence tomography was used to visualize functional vessel normalization. Changes in the same vessel before and after drug treatment were imaged with high resolution in real time. Differences in vascular responses to the mTOR inhibitor rapamycin and to an anti-VEGF antibody were functionally imaged. Tumor vessel normalization was shown by significantly reduced leakiness and subsequent improved tumor delivery of Paclitaxel-BODPY as well as by normalized morphology. The tumor vascular pool agent, AngioSense[750], was retained only in tumors after either anti-VEGF antibody or rapamycin treatment, as visualized by noninvasive fluorescence tomography. The antiangiogenic therapy normalized vessels, which significantly enhanced the antitumor efficacy of paclitaxel because of increased drug penetration throughout the tumor. The optical imaging technology described here is thus a powerful, noninvasive, time-course imaging tool of functional tumor vessel normalization and its therapeutic consequences. *Mol Cancer Ther; 10(7); 1173–84. ©2011 AACR.*

Introduction

Tumor vessel normalization has been proposed as the main mechanism of antitumor efficacy of vascular targeting agents (1, 2). Vascular normalization in the tumor can allow increased drug delivery to the tumor. Normal tumor vasculature may also inhibit the shedding of cancer cells into the circulation, a critical step for metastasis (1).

VEGF promotes the survival and proliferation of endothelial cells (1). VEGF is overexpressed in the majority of solid tumors, and therefore, it was thought that blocking VEGF might revert abnormal tumor vascularity to a more normal state of function (1, 3). Jain (1) initially showed that blockage of VEGF eliminated the immature and leaky vessels of transplanted tumors in mice and remodeled the remaining vasculature. The remolded vasculature more closely resembled normal vasculature. The remodeled vasculature was less leaky, less dilated, and less tortuous with a more normal basement membrane with greater coverage by pericytes. Normalized tumor vascularity results in decreased interstitial fluid pressure, increased tumor oxygenation, and improved penetration of drugs in these tumors (1, 4–11). The normalization window by anti-VEGF antibody treatment is transient and has been found to be approximately 6 days (11).

Tumor vasculature and blood flow are highly heterogeneous. The blood flow distribution, not total blood flow, determines the distribution of a drug or oxygen in tumors (1). Improved imaging techniques are needed to definitively establish the effects of antiangiogenic treatment on vascular structure and function in tumors.

We report here the development of time-course color-coded, noninvasive imaging of functional normalization of tumor vasculature during antiangiogenesis treatment. The imaging technologies used in this report show the role of tumor vascular normalization in enhanced chemotherapeutic drug delivery and antitumor efficacy in the tumor.

Materials and Methods

Cell culture

Human MDA-MB-435-GFP breast cancer cells were generated as previously described (12). The original MDA-MB-435 cell line was obtained from American Type Culture Collection and no authentication was done. Cells

Authors' Affiliations: Departments of [1]Pathology, [2]Medicine, Section of Genetic Medicine and Center for Biomedical Informatics, [3]Cellular and Radiation Oncology, [4]Ludwig Center for Metastasis Research, and [5]Integrated Microscopy Core, The University of Chicago, Chicago, Illinois; [6]AntiCancer, Inc., 7917 Ostrow St., and [7]Department of Surgery, University of California, San Diego, California

Corresponding Author: H. Rosie Xing, Department of Pathology, The University of Chicago, 5841 South Maryland Avenue, AMB N339, MC1089, Chicago, IL 60637. Phone: 773-702-0219; Fax: 773-834-5251; E-mail: hxing@bsd.uchicago.edu

American Association for *Cancer Research*

were maintained in Dulbecco's modified Eagle's medium high glucose supplemented with 10% FBS + 200 μg/mL G418 (Gibco). Cells were subcultured for at least 3 passages before harvesting at their linear growth phase (approximately 70%–80% confluent) for mammary fat pad injection of 5×10^6 cells.

Inhibitors and reagents

Rapamycin, paclitaxel, and anti-VEGF neutralizing antibody were purchased from LC laboratories, Bedford laboratories, or R&D Systems, respectively. Paclitaxel-BODIPY[564/570] and AngioSense[750] probes were obtained from Invitrogen and VisEn, respectively. Lectin was obtained from Vector Laboratories. Antibodies used for immunofluorescence and immunohistochemistry (IHC) were purchased from the following commercial sources: CD31 (BD), α-SMA and NG2 (ABCAM), and Ki-67 (DAKO). The chemical structures of rapamycin, paclitaxel, and paclitaxel-BODIPY[564/570] are provided in Supplementary Fig. S1.

Antiangiogenesis therapy

Drug treatment was initiated when tumor volume reached ~200 to 250 mm³. For determining the efficacy of rapamycin and antihuman VEGF antibody, tumor-bearing animals were randomly divided into 3 treatment groups of 6 to 7 animals as indicated. Rapamycin, freshly dissolved in diluents with 5.2% Tween 80 and 5.2% polyethylene glycol, was administrated daily intraperitoneally (i.p.) at 5 mg/kg/day for 2 weeks. Anti-VEGF neutralizing antibody (5 μg/kg) was given i.p. 3 times a week for 2 weeks. The choice of this dose of VEGF antibody was based on *in vivo* time-course imaging identification of both its vascular normalization and destruction activities, as well as its reported radiosensitization effect (13). Control mice were given equal volumes of PBS, i.p. At the end of the treatment on day 14, animals were sacrificed and tumor tissues were weighed. Tumor samples were collected, either frozen and embedded in optimal cutting temperature compound (Tissue-Tek) for immunofluorescent staining and analysis or fixed in 10% formalin and paraffin embedded for IHC analysis or snap frozen in liquid nitrogen for future quantitative PCR and gene array analysis.

For vessel normalization treatment, alone or in combination with chemotherapy, m.f.p tumor-bearing mice were randomly divided into the following 4 treatment groups: (i) vessel normalization regimen: anti-VEGF antibody (5 μg/kg) was given 3 times (i.p.) for the first week (14, 15), followed by treatment with paclitaxel (15 mg/kg) 3 times a week for 2 additional weeks; (ii) anti-VEGF antibody alone: anti-VEGF (5 μg/kg) was given 3 times (i.p.) for the first week, followed by treatment with vehicle (PBS; i.p.) 3 times a week for 2 additional weeks; (iii) paclitaxel alone: PBS was given (i.p.) 3 times for the first week, followed by treatment with paclitaxel (15 mg/kg) 3 times a week for 2 additional weeks; and

(iv) vehicle control: control tumor-bearing animals were given PBS (i.p.) 3 times a week for 3 weeks.

Variable-magnification *in vivo*-fluorescence imaging

The Olympus OV100 (Olympus Corporation) is equipped with GFP, RFP, and near-infrared (NIR) fluorescence filter sets enabling multichannel coimaging (16, 17). For conducting dual-channel imaging with paclitaxel-BODIPY[564/570] or with the NIR blood pool agent AngioSense[750], the probes were injected via the tail vein 4 hours before imaging (20 and 2 nmol/mouse, respectively). Eight-bit planer images were acquired through the RFP and 750-nm channels of the OV100 similar to what we previously described (16). GFP Z-stacks were obtained between 2 and 4 mm at 10 μm steps at the ×1.6 zoom level. Imaging analysis was conducted by compiling the Z-stack into a 3-dimensional projection image by using ImageJ (NIH).

Fluorescence tomography

The fluorescence-mediated tomography (FMT)1 system (VisEn Medical) is optimized for probes coupled with either 680 nm or the 750 nm channels NIR fluorochromes. The FMT1 system was used for quantifying tumor vessel density in live mice by measuring the tumor uptake of the blood pool probe AngioSense[750] (VisEn Medical) at 4 hours post–tail vein injection. FMT images were acquired by using a continuous wave-type scanner capable of acquiring transillumination, reflectance, and absorption data (VisEn Medical; ref. 18).

Immunofluorescence and immunohistochemistry

Slides with cyrosections were incubated in blocking solution (10% goat serum in 0.1% Triton X-100 PBS) for 1 hour followed by incubation with the first primary antibody (CD31, BD Pharmingen; α-SMA, ABCAM; and NG2, Millipore) diluted 1:100 in blocking solutions at 4°C overnight. After washing, slides were sequentially incubated with the fluorophore-labeled secondary antibody (Molecular Probes) diluted 1:400 in blocking solutions for 30 minutes at room temperature. For vessel staining, 20 μg/mL fluorescein-labeled tomato lectin (Vector Laboratories) was applied to frozen-section slides, which were incubated at 4°C overnight. The slides were then mounted in Vectashield mounting medium with 4′,6-diamidino-2-phenyl-indole (Vector Laboratories). Images were captured and analyzed by using the Zeiss Axiovert 200 and Leica SP-2 confocal microscope.

Quantification of mitotic figures and karyolytic cancer cells

Mitotic figures (MF) were counted in 50 random selected fields for each tumor through a ×40 objective lens of a Lietz light microscope. Similarly, cancer cells that exhibited karyolysis morphology were counted under ×1,000 magnification, and 10 random fields were counted for each tumor.

Statistical analysis

P values were determined by using a single nonparametric Kruskal–Wallis test for all counts across all groups. Because the *P* value was less than 5% (significant), this test was followed by the nonparametric Dunn's Multiple Comparison test comparing all pairs of groups conducted with the statistical software Graphpad Prism version 4.03.

Results

Time-course imaging of tumor vascular morphology, angiogenesis, and function in untreated live mice

We compared VEGF expression among MCF-7, SK-BR3, MDA-MB-435, and MDA-MB-435 cell lines *in vitro* by ELISA assay. Although VEGF production was negligible in MCF-7 and SK-BR3 luminal breast cancer cells, basal MDA-MD-231 cells produced a high level of VEGF (on average 122 pg/mL/100,000 cells). We also detected abundant VEGFA production by cultured MDA-MB-435 cells (on average 56.2 pg/mL/100,000 cells). Because the MDA-MB-435 cells, when injected into the mammary fat pad, yielded more reproducible and angiogenic primary tumors, we chose the MDA-MB-435-GFP imageable model for carrying out the present study. We have confirmed VEGF expression by IHC as well (data not shown).

In the MDA-MB-435-GFP mammary fat pad tumors, the nonluminous capillaries were clearly and noninvasively visible as sharply-defined dark networks against the very bright tumor green fluorescence (Fig. 1). The tumor vessels were tortuous and very abnormal. Pulsatile flow of blood cells could be observed in the smallest capillaries (Supplementary Movie 1).

Four hours after AngioSense[750] injection, the majority of the probe was seen contained within the tumor blood vessels. However, AngioSense[750] retention was primarily lost at 24 hours postinjection (Fig. 1B). In contrast, normal skin blood vessel retained Angiosense[750] at this time point (data not shown). This observation indicates that the tumor vasculature of MDA-MB-435, as seen in real time at multiple time points in individual mice, was highly permeable and leaky. This is consistent with previous reports (2, 18–22).

Tumor angiogenesis progression in the MDA-MB-435 tumor was visualized via sequential imaging of the same tumor at indicated time points of tumor growth. Angiogenesis in this tumor is characterized by recruitment of existing blood vessels into the tumor bed (Fig. 1D), blood island formation (Fig. 1D), angiogenic sprouting (Fig. 1D), and formation of a fully established tumor vasculature network (Fig. 1D; days 48 and 55). As the tumor vasculature matured, the imaging depth increased significantly from 300 μm (tumor volume: ~120 mm³) to 4 mm (tumor volume: >250 mm³). High-resolution GFP Z-stack images could also be obtained at ×0.89 or ×1.6 magnification and reconstructed for 3-dimensional visualization [Supplementary Fig. S2(i)].

Imaging tumor vascular response to antiangiogenic therapies

In untreated tumors, torturous, thin vessels of uneven size with abrupt ends were visualized (Fig. 2A, i, iv, and vii; refs. 23–25). Shown in Fig. 2A are representative OV100 sequential images of 1 tumor from each treatment group during the 2-week observation period. The observed vascular changes are highly reproducible and consistent among the multiple tumors imaged for each group and between independent experiments. Within the PBS-treated control tumors, when tumor volume increased from 250 to over 400 mm³, tumor vessels close to the tumor surface (imaging depth ~4 mm) appeared increasingly more distended and dilated (Fig. 2A, i–iii; ×2), suggesting increased intratumor pressure, possibly caused by high permeability of the tumor vessels (Fig. 1B) and poor lymphatic drainage (26, 27).

Seven days of rapamycin treatment led to destruction of fine microvessels, leaving larger vessels mostly intact but extremely dilated (Fig. 2A, iv–v). In addition, induction of small but visible tumor surface necrosis, associated with vessel destruction, was observed (data not shown). Loss of both microvessels and large vessels was accelerated with prolonged rapamycin treatment for 7 additional days and the necrotic area was also enlarged (Fig. 2A, vi vs. Fig. 2A, v).

In contrast, anti-VEGF antibody treatment in the first 7 days produced no significant vessel destruction (Fig. 2A, vii vs. Fig. 2A, viii), whereas the degree of vessel dilation observed was similar to the control tumors (Fig. 2A, viii vs. Fig. 2A, ii). However, prolonged anti-VEGF antibody treatment elicited a robust vessel damage response, as evident by the loss of both micro- and large vessels on day 14 (Fig. 2A, ix). At the end point, vessel loss was comparable between rapamycin and anti-VEGF antibody treatment (Fig. 2A, vi vs. Fig. 2A, ix). However, the kinetics differed significantly. The observed differences in vascular response to rapamycin and anti-VEGF could have been missed if time-course imaging had not been conducted. Although the 2-week anti-VEGF antibody or rapamycin treatments caused significant damage to the preexisting tumor vasculature, normal vessels in the skin near the mammary fat pad were not affected by the drug treatment (data not shown).

Further, treatment-induced morphologic vascular changes and tumor blood vessel damage could be more vividly visualized in 3 dimensions when Z-stack OV100 planar images were processed and reconstructed (Fig. 2A, x–xii; Supplementary Fig. S2 for enlarged images).

To image deeper in the tumor, we also conducted confocal immunoflourescence microcopy (Supplementary Methods) on MDA-MB-435 frozen tumor sections to determine whether the vascular changes detected relatively close to the tumor surface via *in vivo* imaging reflect overall tumor vascular alterations. Significant tumor vessel loss in nonnecrotic areas of the tumor core was detected in response to both anti-VEGF and rapamycin therapy (Fig. 2A).
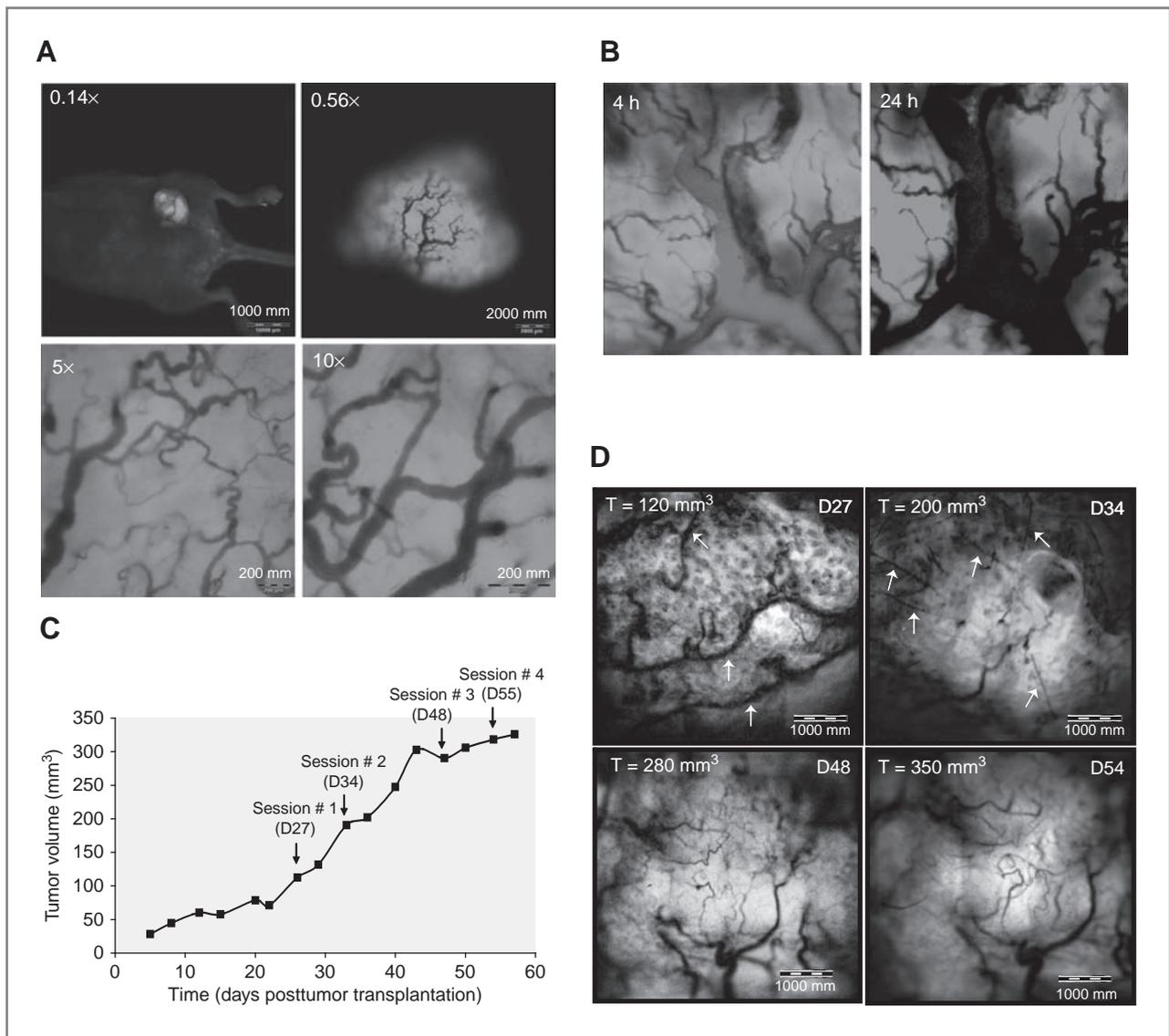
Figure 1. Noninvasive time-course imaging of the development of tumor vascular network in live mice. A, MDA-MB-435-GFP mammary fat pad tumor vessels visualized through skin with subzoom ($\times$0.14 and $\times$0.56) and zoom magnification ($\times$5 and $\times$10) of the OV100 imaging system in the absence of a blood vessel contrast agent. B, AngioSense[750] (18) was used to visualize tumor vascular permeability over time. AngioSense[750] was retained within the tumor vessels at 4 hours and leaked out 24 hours after injection. C, noninvasive sequential imaging sessions were conducted at the indicated time points during the linear phase of tumor growth. D, four representative images taken from 1 tumor on days 27, 34, 48, and 55 after tumor transplantation, showing the progression of tumor angiogenesis. Reproducible observations were obtained from tumors in the same experiments and from one experiment to the other.

A second *in vivo* imaging modality, FMT, was used to visualize tumor vascular response to antiangiogenic therapy. AngioSense[750] NIR dye tumor uptake was used as an indirect measure of tumor vascular volume (17, 22, 28). In Fig. 2B, one representative z-slice (at 260 μm from the tumor surface) showed both qualitative and quantitative differences between AngioSense[750] tumor uptake in PBS-treated control tumors and in tumors receiving 14 days of either rapamycin or anti-VEGF antibody treatment. There was significantly reduced vascular uptake of AngioSense[750] in rapamycin-treated

tumors over 2 weeks (Fig. 2B, iii and iv) as well as by anti-VEGF antibody-treated tumors (Fig. 2B, v and vi, respectively).

Efficacy of combined antiangiogenic treatment on tumor growth

We also characterized tumor growth response to the 2 therapies. Although anti-VEGF antibody treatment led to significant vascular changes (Fig. 1A), it did not inhibit tumor growth (Fig. 2C). In contrast, rapamycin treatment effectively halted tumor growth and even initiated tumor

regression from day 10 of treatment and onward (Fig. 2C). Consistent with the lack of tumor growth inhibition by anti-VEGF antibody treatment (Fig. 2C), cancer-cell proliferation measured by MFs (Fig. 2D, i) remained as high in anti-VEGF antibody treated tumors as that of the control tumors (6.8 ± 0.5 in control tumors vs. 5.4 ± 0.6 in anti-VEGF antibody treated tumors; Fig. 2D, ii). In contrast, rapamycin treatment significantly inhibited MDA-MB-435 cancer cell proliferation (MF = 2.5 ± 0.3; $P < 0.0001$; Fig. 2D, ii). The quantitative differences in MF between anti-VEGF antibody and rapamycin treatments were confirmed by IHC staining of the cell proliferation marker Ki67 (Fig. 2D, i, iv–vi). Rapamycin directly inhibited MDA-MB-435-GFP cell proliferation *in vitro* as well (Fig. 2D, iii).

We also observed widespread induction of karyolysis, a form of necrosis characterized by the dissolution of the nucleus, only in rapamycin-treated tumors (Fig. 2E). Karyolytic cells were only rarely found in the control and in anti-VEGF antibody-treated tumors (data not shown). Quantitative differences of karyolytic necrosis between rapamycin-treated tumors and control were significant ($P = 0.003$; Fig. 2E). The even distribution of karyolytic cells throughout the rapamycin-treated tumor suggests that the delivery of rapamycin was likely uniform and penetrated deep into the tumor center.

Antiangiogenic treatment results in reduced tumor vascular permeability

We examined the effect of anti-VEGF antibody and rapamycin treatments on vascular permeability of MDA-MB-435 tumor vessels. At 4 hours, AngioSense[750] was seen mostly within the tumor blood vessels, and there were no apparent differences among different treatment groups (Fig. 3A). However, at 24 hours post-AngioSense[750] injection, the probe leaked out of the vessels of control tumors (Fig. 3A, iv vs. i; red). When imaged at higher magnification ($\times 10$ digital zoom) in control tumors, AngioSense[750] was found to mostly accumulate in patches adjacent to blood vessels with minimal distribution into tumor parenchyma [Fig. 3B(i–iii)]. Upon treatment with anti-VEGF antibody or rapamycin for 2 weeks, although significant vascular damage was observed (Fig. 2A–B), the aberrant hyperpermeability of blood vessels in MDA-MB-435 tumors (Fig. 1B) was greatly reduced in the nondamaged remaining microvessels. This was evident by extensive AngioSense[750] vessel retention at 24 hours postprobe injection (Fig. 3A, ii vs. v and iii vs. vi). AngioSense[750] also penetrated more evenly into the tumor parenchyma surrounding the blood vessels in the treated tumors (Fig. 3B, iv–vi; and data not shown).

## Antiangiogenesis treatment increased pericyte coverage of tumor vessels

We then tested whether rapamycin and anti-VEGF antibody treatments also normalized the wall structure of the blood vessels (29, 30), in particular the associa-

tion of pericytes with tumor vessels. Therefore, we first determined the expression of alpha smooth muscle antigen (α-SMA), a marker for mature pericytes in control and treated tumors by using IHC (Fig. 3C, i–iii). Tumor vessels in PBS-treated control tumors were sparsely decorated with α-SMA-positive cells and the coverage for a given area of vessel was disjointed and short (Fig. 3A, i). In comparison, α-SMA staining in rapamycin or anti-VEGF antibody-treated tumors was much more intense (Fig. 3A, ii vs. i). α-SMA-positive cells were found to line the outside of blood vessels (Fig. 3A, iv) similar to pericytes. Increased perivascular α-SMA expression in the treated tumors, detected by IHC analysis, was confirmed by α-SMA immunofluorescence staining by using frozen tumor sections (Fig. 3C, v; Supplementary Fig. S3). An increase in α-SMA-positive mature pericytes after drug treatment was further confirmed by an increase of NG2 immunofluorescence staining, a specific marker for less mature pericytes (Fig. 3C, vi; Supplementary Fig. S3). Additionally, confocal scanning microscopy was conducted to acquire high-resolution Z-stack images that were subsequently reconstructed in 3 dimensions to characterize α-SMA and NG2 staining, respectively (Fig. 3C, v and vi). This method allowed the visualization of the close association between pericytes and tumor microvessels, as well as the improved coverage of tumor vessels by pericytes in treated tumors. Consistent with vessel normalization, blood vessels exhibited an increase in the width of periodic acid-Schiff (PAS; Alcian blue) staining for basement membrane in the treated tumors (Fig. 3C, vii–viii, arrows).

Combination of antiangiogenic and chemotherapy results in improved antitumor efficacy

We assessed whether normalization of the tumor vascular network, in particular reducing vascular hyperpermeability, resulted in increased chemotherapy drug distribution in the tumor. Tumor vascular damage over time was quantified using a lectin angiogram (Fig. 4A). These results show that vascular changes visualized and characterized by *in vivo* imaging (Fig. 2) accurately reflect the whole tumor vascular response.

We injected a subtherapeutic dose of BODPY-labeled paclitaxel (564/570) as a fluorescent imaging tracer to visualize tumor drug distribution (Fig. 4B). In PBS-treated tumors, 4 hours after injection, paclitaxel-BODIPY already leaked out of the blood vessels and accumulated in patches near the vessels (Fig. 4B, i–iii). In contrast, in anti-VEGF antibody-treated tumors, the majority of paclitaxel-BODIPY was evenly distributed throughout the tumor parenchyma (Fig. 4B, iv–vii), although vessel retention was also observed (data not shown). Increased tumor drug delivery efficiency, visualized in live mice, was confirmed by scanning confocal microscopic imaging of cancer cell paclitaxel-BODIPY uptake in frozen sections (Fig. 4C). In PBS-treated control tumors, paclitaxel-BODIPY distribution was limited to the tumor
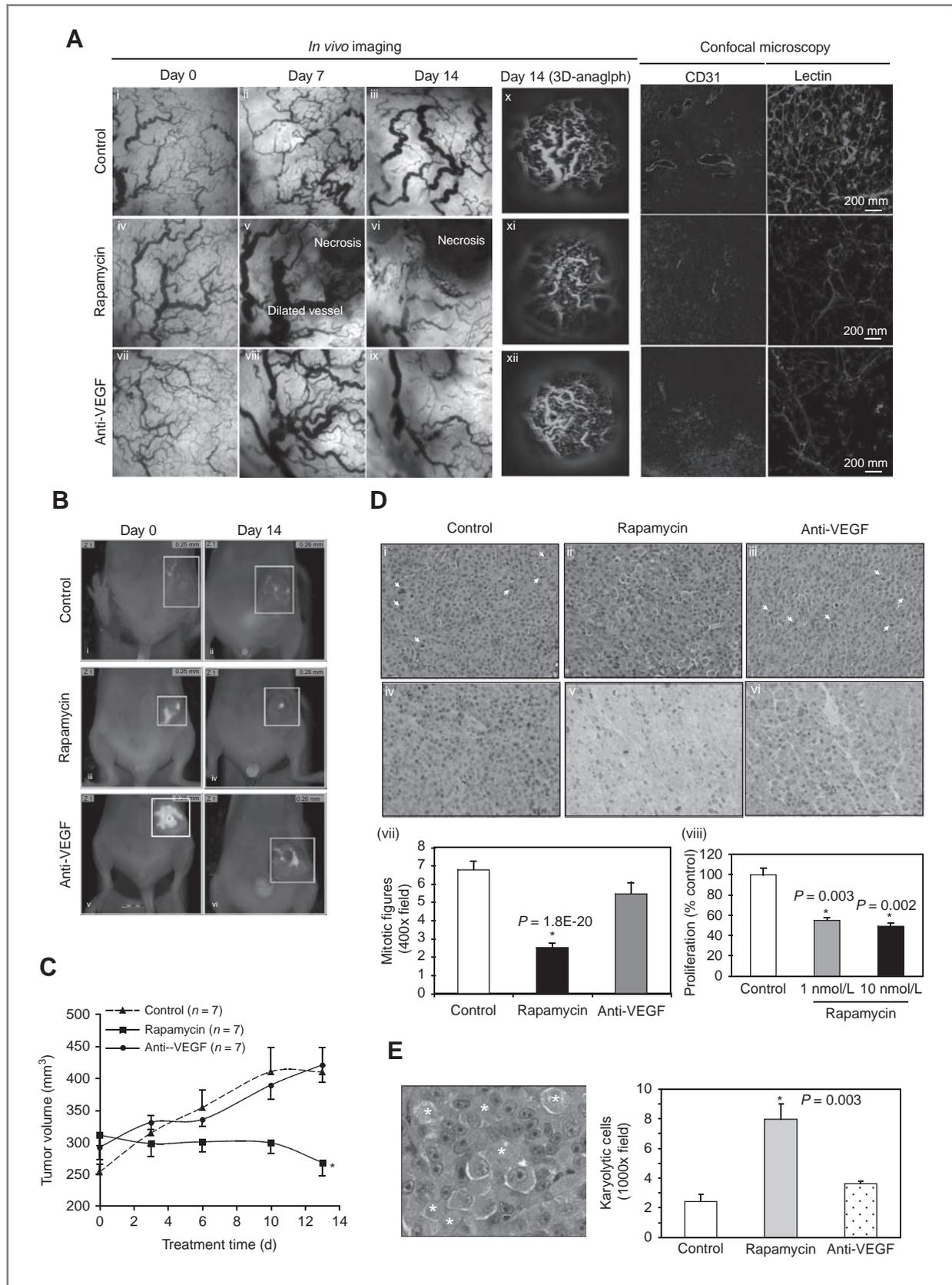
surface (Fig. 4C, i) and was totally absent in the tumor core (Fig. 4C, ii). In contrast, in tumors treated with anti-VEGF and paclitaxel-BODIPY, drug distribution was observed throughout the viable areas of the whole tumor (Fig. 4C, iii and iv). Cancer cell-bound paclitaxel-BODIPY was clearly seen at higher magnification (Fig. 4C, v).

Treatment with anti-VEGF antibody alone for 1 week (schedule #2) or paclitaxel alone for 2 weeks (schedule #3) exhibited a very mild tumor growth inhibitory effect compared with PBS-treated tumors on day 20 (Fig. 5A, ii). In contrast, 1 week of antiangiogenic therapy followed by 2 weeks of paclitaxel chemotherapy effectively halted tumor growth, resulting in enhancement of antitumor activity compared with treatment with each agent alone ($P < 0.05$; Fig. 5A, ii and iii; $P = 0.01$). Moreover, neither significant body weight loss nor other visible toxicity to the mice was observed among these treatment groups (data not shown).

The number of MFs was considerably reduced in tumors that received combination treatment (MF = 3.0 ± 0.4 vs. 7.2 ± 0.2 for the control tumors; $P < 0.001$; Fig. 5B, v). Coagulating necrotic foci or cancer cells exhibiting mild degeneration changes, that is, karyolysis, or swollen and hydrated cytoplasm (Fig. 5B, i; data not shown) were rare in untreated tumor tissues. In contrast, combination therapy-treated tumors contained more cells with severe degenerative damage including cytoplasm and nuclear hydration, karyolysis, as well as multinucleated giant cells (Fig. 5B, ii). These degenerative changes were more pronounced in tumors treated with combination therapy (Fig. 5B, iv and v). The observed antiproliferative effect of combination treatment of cancer cells within tumors was consistent with in vitro dose-dependent inhibition of MDA-MB-435 cell growth by paclitaxel (Fig. 5B, vi).

To characterize the vascular effect of antiangiogenic induction therapy in combination with paclitaxel, we stained frozen tumor sections with the endothelial cell marker CD31 (Fig. 5C). CD-31–positive tumor vessels in nonnecrotic tumor regions of the combination therapy-treated tumors appeared highly dilated (Fig. 5C, iii), suggesting improved tumor microcirculation with paclitaxel treatment.

Discussion

The combined imaging technologies used in this study have provided a more complete understanding of mechanisms of functional vascular response to antiangiogenesis agents and how to maximize their antitumor efficacy. Moreover, in vivo imaging observations were thoroughly validated and confirmed with histologic and immunofluorescence staining analyses along with scanning confocal microscopy.

For a cytotoxic agent to be effective, it must reach all cancer in effective quantities in tumors. The abnormally high leakiness of tumor vasculature hinders drug delivery by inducing blood flow stasis (31). Our data provide, for the first time, time-course visualization of transient tumor vessel functional normalization. We used this window of normalization for the design of an effective antiangiogenic and chemotherapy combination that improved the antitumor efficacy of paclitaxel by greatly increasing tumor drug penetration and cancer cell uptake. Our observations support the concept of vascular normalization by antiangiogenesis drugs (1, 2), and show that judicious application of antiangiogenic treatment can functionally normalize the tumor vasculature as well as facilitate a more uniform delivery of therapeutic agents to cancer cells. Prolonged treatment with a subclinical dose of anti-VEGF antibody led to functional vessel normalization, which enhanced the antitumor efficacy of paclitaxel.

We also observed increased pericyte association with tumor vessels that accompanied functional normalization, by using IHC and immunofluorescence analysis after treatment with rapamycin and anti-VEGF antibody. Future studies are required to determine whether the increase in the number of SMA- and NG2-expressing mural cells is because of induction of SMA- and NG2 expression by preexisting immature mural cells in the tumor, or results from increased proliferation of a small number of mural cells in response to treatment with antiangiogenic agents. Additionally, whether the effect of antiangiogenic treatments on mural/pericytes is common among different models with varying amount of

Figure 2. Noninvasive time-course imaging and characterization of tumor vascular response to antiangiogenesis therapy. A, three sequential OV100 imaging sessions were conducted on days 0, 7, and 14 of the 2-week treatment period. Imaging fields of interest were identified on day 0 and the same imaging field was localized and characterized for subsequent imaging during the course of treatment. In vivo imaging observations of changes in vessel density were confirmed with CD31 staining and lectin angiograms by using scanning confocal microscopy. B, AngioSense[750] uptake in a tumor at 4 hours postinjection, by using the VisEn FMT, correlated with tumor vessel volume. C, tumor growth curve during the 2-week treatment period. Rapamycin versus control had a $P < 0.05$ (*). The P values were calculated by using 1-way ANOVA (Supplementary Methods). D and E, examination of dissected tumor by hematoxylin and eosin (H&E) staining revealed that rapamycin significantly inhibited cancer cell mitosis and caused widespread karyolysis. However, anti-VEGF antibody did not kill cancer cells. D, i–vi, histologic examination of dissected tumors showed that rapamycin significantly inhibited cancer cell mitosis (D, i–iii; top; white arrows) and proliferation (D, iv–vi; bottom; Ki67 staining). D, vii, MF counts in the epithelial component of the cancerous tissue were identified. MFs in 50 random HPFs (×40) were counted for each tumor and 5 tumors were scored (Supplementary Methods). The P values were determined by using a single nonparametric Kruskal–Wallis test, followed by Dunn's multiple comparison test (Supplementary Methods). D, viii, rapamycin treatment significantly (*) inhibited MDA-MB-435-GFP cell proliferation in vitro. P values were determined with the 2-tailed unequal variance Student's t-test. E, rapamycin treatment caused widespread karyolysis (left; H&E; asterisks), but anti-VEGF antibody lacks such activity. Cancer cells that exhibited karyolysis were counted under ×100 magnification, and 10 random fields were counted from each tumor (right). A total of 5 tumors (50 HPFs) from each treatment group were used for quantitative and statistical analysis. The P values were determined with the 2-tailed unequal variance Student's t-test.
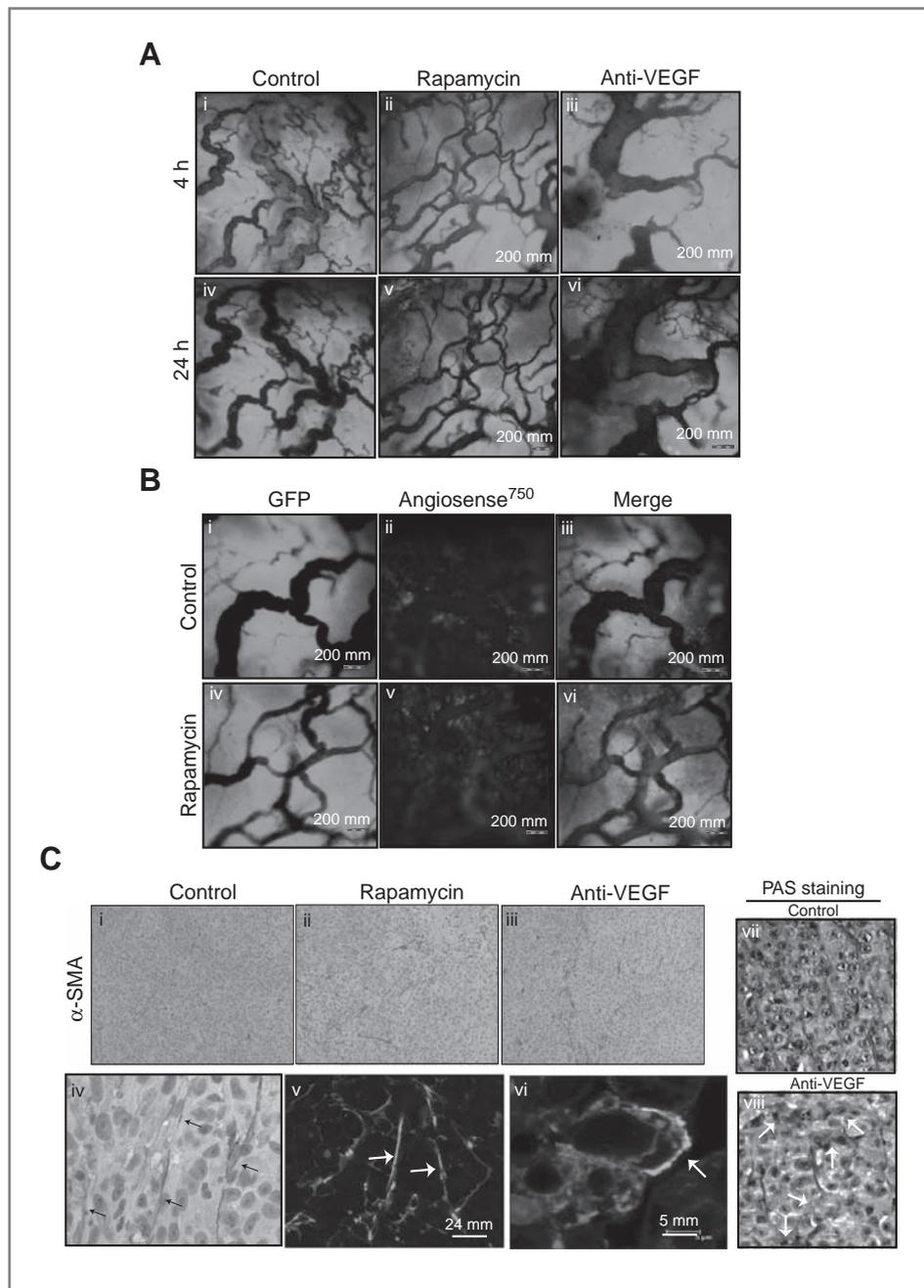
Figure 3. Antiangiogenic treatment improved tumor vascular hyperpermeability and increased pericyte coverage of tumor vessels. A, vascular permeability and leakage were visualized by retention of AngioSense[750]. AngioSense[750] (18) was injected and imaged with the OV100 (480 nm GFP and 750 nm NIR channels) at 4 hours (i–iii) and 24 hours (iv–vi) after probe injection. B, at higher magnification (×6), AngioSense[750] was found to mostly accumulate in patches near vessels in control tumors (top), whereas it diffused more evenly into tumor parenchyma in rapamycin-treated tumors (bottom). C, expression markers for pericytes were significantly increased in rapamycin and anti-VEGF antibody-treated tumors. The expression of α-SMA was determined in control and treated tumors via IHC analysis (i–iv) and immunofluorescence staining (v; Supplementary Fig. S3). An increase in α-SMA positive mature pericytes after drug treatment was confirmed by an increase of NG2 immunofluorescence staining (29), a specific marker for less mature pericytes (vi; Supplementary Fig. S3). The perivascular basement membrane was visualized by PAS staining (vii–viii). Reproducible observations were obtained from tumors in the same experiments and from one experiment to the other.

mural cell distribution merits further investigation, which will be carried out in a future study.

We have showed the direct vascular targeting effect of antiangiogenic treatment by lectin staining (Fig. 2A) and also by CD31 staining (Fig. 5C). The proliferation of endothelial cells, by using markers such as Ki67, during antiangiogenesis treatment will be determined in future studies.

It is noteworthy the low dose (5 μg/kg) of anti-VEGF antibody we used was much lower than the vessel-destroying high doses (5–10 mg/kg) reported in the literature. The low dose was initially chosen based on its significant effect on radiosensitization (13). We showed the vascular normalization and destruction activities of the low dose by time-course imaging.

Because of the lack of antitumor growth effect of this low dose of anti-VEGF antibody, the robust vascular normalizing effect at the low dose of drug used in the study would have been missed if time-course imaging were not carried out. Although low-dose anti-VEGF antibody treatment did not affect tumor growth, it was sufficient to achieve chemosensitization, similar to the

Figure 4. Paclitaxel uptake increased upon normalization of tumor vessel function. A, tumor vessel normalization was identified by scanning confocal microscopy (i) and quantification (ii–iii) of tumor vessel density through lectin staining (29) at indicated time points of anti-VEGF antibody treatment. B, tumor distribution of paclitaxel-BODIPY$^{564/570}$ was visualized via dual channel OV100 time-course imaging. Paclitaxel-BODIPY was evenly distributed throughout the tumor parenchyma with normalized vasculature. i–vi, digital zoom (×10); vii, ×6.6 digital zoom. Scale bars, 200 μm. C, improved drug delivery after vessel normalization was further confirmed by scanning confocal microscopy analyses of paclitaxel-BODIPY tumor distribution near the tumor surface (i and iii) and in the tumor core (ii and iv) seen in frozen tumor sections. High magnification confocal imaging showed uptake of paclitaxel-BODIPY by single tumor cells (v). Scale bars, 40 μm in i–iv; 10 μm in v.
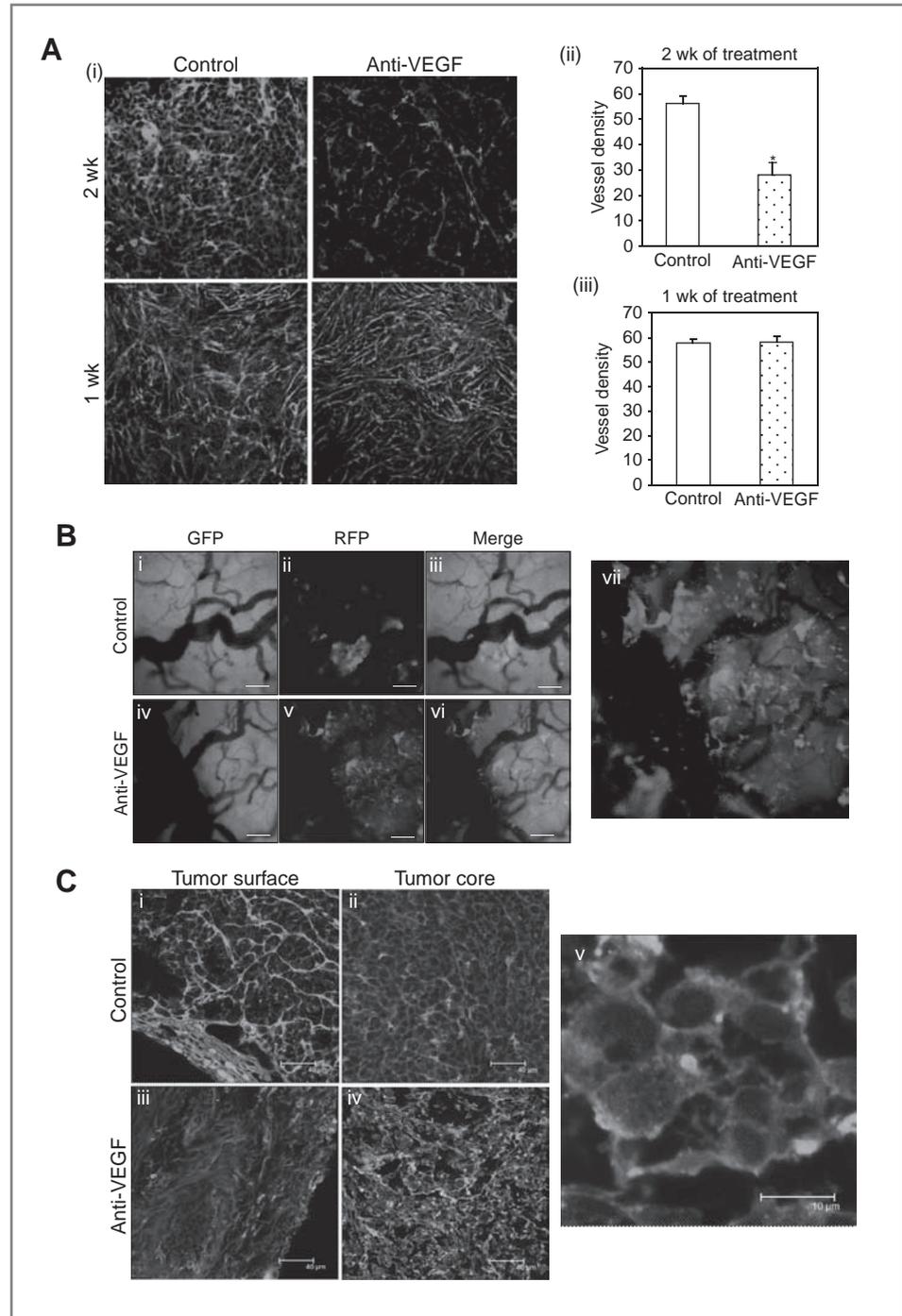
radiosensitization effect by using the identical low dose (13). These results indicate that antiangiogenic therapy could be used at a deintensified dosing schedule to achieve vessel normalization and chemosensitization.

Recently, using a high dose of anti-VEGF antibody, Yanagisawa and colleagues (32) observed that the combination of anti-VEGF antibody and paclitaxel had antitumor activity, reduced microvessel density, and decreased vascular permeability. In contrast to Yanagisawa and colleagues (32), which used excised tissue for analysis from an ectopic mouse model, the results presented in this report show, in an orthotopic mouse model, that the noninvasive imaging platforms we developed afford real-time assessment in living mice of the 3-dimensional physical and functional properties of tumor vascular normalization. In addition, imaging showed the
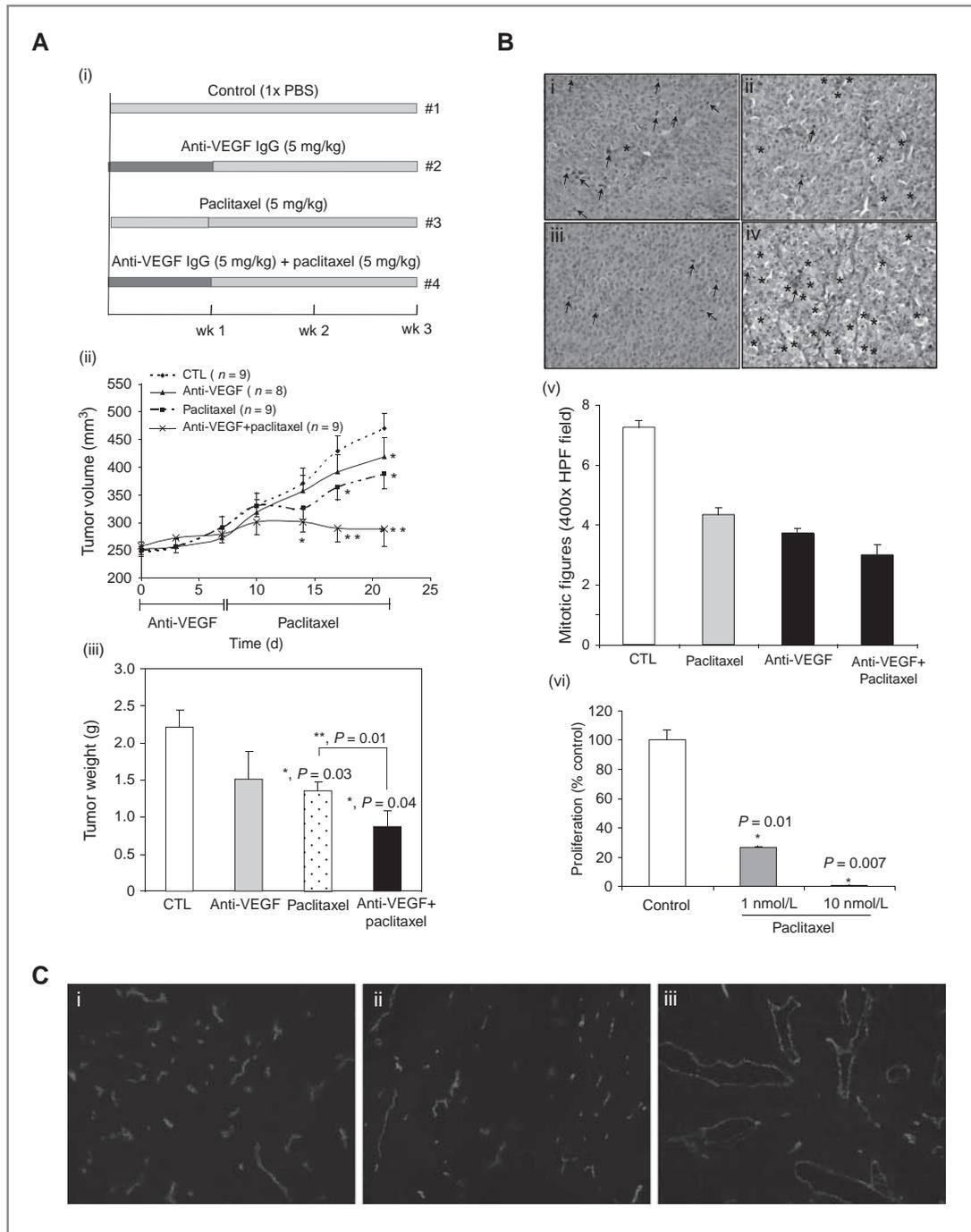
Figure 5. Optimization of paclitaxel efficacy after normalization of tumor vessel function by antiangiogenesis therapy. A, antiangiogenesis therapy significantly enhanced the antitumor efficacy of paclitaxel. A, i, experimental design (Supplementary Methods). A, ii, tumor growth curves of 4 different treatments over 3 weeks. *, $P < 0.05$ at indicated time points compared with control tumor (CTL) volume; **, $P < 0.05$ for the combination treatment at the indicated time points compared with both control and with single-agent treatment. A, iii, tumor weight measurement at experimental end points. The P values were determined with the 2-tailed unequal variance Student's t-test. B, examination of dissected tumors by H&E staining revealed that rapamycin significantly inhibited cancer cell mitosis and caused widespread karyolysis as well as degenerative cell damage. B, i–iv, visualization of MFs and karyolysis in tumors receiving different treatments. i, control; ii, paclitaxel; iii, anti-VEGF antibody; iv, anti-VEGF antibody + paclitaxel. Arrows, MFs; asterisks, karyolytic and degenerative cells. B, v, MF counts in the epithelial component of tumors were identified. MFs in 50 random HPFs (×40) were counted for each tumor and 5 tumors were scored (Supplementary Methods). The P values were determined by using a single nonparametric Kruskal–Wallis test, followed by Dunn's multiple comparison test (Supplementary Methods). B, vi, paclitaxel treatment significantly (*) inhibited MDA-MB-435-GFP cell proliferation in vitro. The P values were determined with the 2-tailed unequal variance Student's t-test. C, ntiangiogenic therapy enhances efficacy of paclitaxel. Tumor vessel density was visualized by scanning confocal microscopy of CD-31 staining (24). i, paclitaxel treatment (treatment protocol #3); ii, anti-VEGF antibody treatment (treatment protocol #2); iii, anti-VEGF antibody + paclitaxel (treatment protocol #4).

increased distribution of drug in the tumor after vascular normalization was effected, suggesting this is the basis for increased drug efficacy. Each animal serves as its own control when noninvasive imaging is used to follow functional tumor vascular normalization and drug efficacy. This is a major improvement from sacrificing mice at each time point and comparing the results with different mice (32–35).

In summary, we have developed a noninvasive imaging model to identify effective antiangiogenic therapeutic strategies that result in antitumor efficacy. Time-course imaging showed that vascular normalization was affected by low-dose anti-VEGF antibody and also showed the change in pattern in delivery of paclitaxel to the cells in the tumor was affected by vascular normalization. Development of combination therapy that links angiogenic responses to chemotherapy opens a new paradigm of effective cancer therapy. The imaging model

and technology described here can play an important role in developing such effective therapy.

Disclosure of Potential Conflicts of Interest

Grant Support

References

1. Jain RK. Normalization of tumor vasculature: an emerging concept in antiangiogenic therapy. Science 2005;307:58–62.
2. O'Connor JP, Jackson A, Parker GJ, Jayson GC. DCE-MRI biomarkers in the clinical evaluation of antiangiogenic and vascular disrupting agents. Br J Cancer 2007;96:189–95.
3. Yuan F, Chen Y, Dellian M, Safabakhsh N, Ferrara N, Jain RK. Time-dependent vascular regression and permeability changes in established human tumor xenografts induced by an antivascular endothelial growth factor/vascular permeability factor antibody. Proc Natl Acad Sci U S A 1996;93:14765–70.
4. Hobbs SK, Monsky WL, Yuan F, Roberts WG, Griffith L, et al. Regulation of transport pathways in tumor vessels: role of tumor type and microenvironment. Proc Natl Acad Sci U S A 1998;95:4607–12.
5. Teicher BA. A systems approach to cancer therapy. (Antioncogenics + standard cytotoxics–>mechanism(s) of interaction). Cancer Metastasis Rev 1996;15:247–72.
6. Lee CG, Heijn M, di Tomaso E, Griffon-Etienne G, Ancukiewicz M, Koike C, et al. Antivascular endothelial growth factor treatment augments tumor radiation response under normoxic or hypoxic conditions. Cancer Res 2000;60:5565–70.
7. Tong RT, Boucher Y, Kozin SV, Winkler F, Hicklin DJ, Jain RK. Vascular normalization by vascular endothelial growth factor receptor 2 blockade induces a pressure gradient across the vasculature and improves drug penetration in tumors. Cancer Res 2004;64:3731–6.
8. Kadambi A, Mouta Carreira C, Yun CO, Padera TP, Dolmans DE, Carmeliet P, et al. Vascular endothelial growth factor (VEGF)-C differentially affects tumor vascular function and leukocyte recruitment: role of VEGF-receptor 2 and host VEGF-A. Cancer Res 2001;61:2404–8.
9. Inai T, Mancuso M, Hashizume H, Baffert F, Haskell A, Baluk P, et al. Inhibition of vascular endothelial growth factor (VEGF) signaling in cancer causes loss of endothelial fenestrations, regression of tumor vessels, and appearance of basement membrane ghosts. Am J Pathol 2004;165:35–52.
10. Wildiers H, Guetens G, De Boeck G, Verbeken E, Landuyt B, Landuyt W, et al. Effect of antivascular endothelial growth factor treatment on the intratumoral uptake of CPT-11. Br J Cancer 2003;88:1979–86.
11. Winkler F, Kozin SV, Tong RT, Chae S, Booth MF, Garkavtsev I, et al. Kinetics of vascular normalization by VEGFR2 blockade governs brain tumor response to radiation: role of oxygenation, angiopoietin-1, and matrix metalloproteinases. Cancer Cell 2004;6:553–63.
12. Li X, Wang J, An Z, Yang M, Baranov E, Jiang P, et al. Optically imageable metastatic model of human breast cancer. Clin Exp Metastasis 2002;19:347–50.

13. Gupta VK, Jaskowiak NT, Beckett MA, Mauceri H, Grunstein J, Johnson R, et al. Vascular endothelial growth factor enhances endothelial cell survival and tumor radioresistance. Cancer J 2002;8:47–54.
14. Cao Q, Li ZB, Chen K, Wu Z, He L, Neamati N, et al. Evaluation of biodistribution and antitumor effect of a dimeric RGD peptide-paclitaxel conjugate in mice with breast cancer. Eur J Nucl Med Mol Imaging 2008;35:1489–98.
15. Volk LD, Flister MJ, Bivens CM, Stutaman A, Desai N, Trieu V, et al. Nab-paclitaxel efficacy in the orthotopic model of human breast cancer is significantly enhanced by concurrent antivascular endothelial growth factor A therapy. Neoplasia 2008;10:613–23.
16. Yamauchi K, Yang M, Jiang P, Xu M, Yamamoto N, Tsuchiya H, et al. Development of real-time subcellular dynamic multicolor imaging of cancer-cell trafficking in live mice with a variable-magnification whole-mouse imaging system. Cancer Res 2006;66:4208–14.
17. Zhang Q, Yang M, Shen J, Gerhold LM, Hoffman RM, Xing HR. The role of the intravascular microenvironment in spontaneous metastasis development. Int J Cancer 2010;126:2534–41.
18. Montet X, Figueiredo JL, Alencar H, Ntziachristos V, Mahmood U, Weissleder R. Tomographic fluorescence imaging of tumor vascular volume in mice. Radiology 2007;242:751–8.
19. Zhang Q, Fan H, Shen J, Hoffman RM, Xing HR. Human breast cancer cell lines coexpress neuronal, epithelial, and melanocytic differentiation markers *in vitro* and *in vivo*. PLoS One 2010;5:e9712.
20. Bachelder RE, Crago A, Chung J, Wendt MA, Shaw LM, Robinson G, et al. Vascular endothelial growth factor is an autocrine survival factor for neuropilin-expressing breast carcinoma cells. Cancer Res 2001;61:5736–40.
21. Bachelder RE, Wendt MA, Mercurio AM. Vascular endothelial growth factor promotes breast carcinoma invasion in an autocrine manner by regulating the chemokine receptor CXCR4. Cancer Res 2002;62:7203–6.
22. Hanyu A, Kojima K, Hatake K, Nomura K, Murayama H, Ishikawa Y, et al. Functional *in vivo* optical imaging of tumor angiogenesis, growth, and metastasis prevented by administration of antihuman VEGF antibody in xenograft model of human fibrosarcoma HT1080 cells. Cancer Sci 2009;100:2085–92.
23. Lane HA, Wood JM, McSheehy PM, Allegrini PR, Boulay A, Brueggen J, et al. mTOR inhibitor RAD001 (everolimus) has antiangiogenic/vascular properties distinct from a VEGFR tyrosine kinase inhibitor. Clin Cancer Res 2009;15:1612–22.
24. Jain RK, Tong RT, Munn LL. Effect of vascular normalization by antiangiogenic therapy on interstitial hypertension, peritumor edema,

and lymphatic metastasis: insights from a mathematical model. Cancer Res 2007;67:2729–35.

25. Stohrer M, Boucher Y, Stangassinger M, Jain RK. Oncotic pressure in solid tumors is elevated. Cancer Res 2000;60:4251–5.

26. Jain RK. Normalizing tumor vasculature with antiangiogenic therapy: a new paradigm for combination therapy. Nat Med 2001;7:987–9.

27. Wurdinger T, Tannous BA, Saydam O, Skog J, Grau S, Soutschek J, et al. miR-296 regulates growth factor receptor overexpression in angiogenic endothelial cells. Cancer Cell 2008;14:382–93.

28. Morikawa S, Baluk P, Kaidoh T, Haskell A, Jain RK, McDonald DM. Abnormalities in pericytes on blood vessels and endothelial sprouts in tumors. Am J Pathol 2002;160:985–1000.

29. Greenberg JI, Shields DJ, Barillas SG, Acevedo LM, Murphy E, Huang J, et al. A role for VEGF as a negative regulator of pericyte function and vessel maturation. Nature 2008;456:809–13.

30. Jain RK, Munn LL, Fukumura D. Dissecting tumor pathophysiology using intravital microscopy. Nat Rev Cancer 2002;2:266–76.

31. Baish JW, Netti PA, Jain RK. Transmural coupling of fluid flow in microcirculatory network and interstitium in tumors. Microvasc Res 1997;53:128–41.

32. Yanagisawa M, Yorozu K, Kurasawa M, Nakano K, Furugaki K, Yamashita Y, Mori K, et al. Bevacizumab improves the delivery and efficacy of paclitaxel. Anti-Cancer Drugs 2010;21:687–94.

33. Katz MH, Bouvet M, Takimoto S, Spivack D, Moossa AR, Hoffman RM. Selective antimetastatic activity of cytosine analog CS-682 in a red fluorescent protein orthotopic model of pancreatic cancer. Cancer Res 2003;63:5521–5.

34. Katz MH, Takimoto S, Spivack D, Moossa AR, Hoffman RM, Bouvet M. A novel red fluorescent protein orthotopic pancreatic cancer model for the preclinical evaluation of chemotherapeutics. J Surg Res 2003;113:151–60.

35. Amoh Y, Li L, Yang M, Moossa AR, Katsuoka K, Penman S, et al. Nascent blood vessels in the skin arise from nestin-expressing hair-follicle cells. Proc Natl Acad Sci U S A 2004;101:13291–5.